

A prolific repeating fast radio burst source and a crisis of the magnetar model

Jun-Shuo Zhang^{1,2†}, Tian-Cong Wang^{3,4†}, Pei Wang^{1,4,5*}, He Gao^{3,4*}, Qin Wu⁶,
 Di Li^{7,1,5*}, Weiwei Zhu^{1,4,5*}, Bing Zhang^{8,9,10*}, Ke-Jia Lee^{11,1,12,13}, Jinlin Han^{1,2,5},
 Chao-Wei Tsai^{1,4,2,5}, Fayin Wang^{6,14}, Yong-Feng Huang^{6,14}, Yuan-Chuan Zou¹⁵,
 Dengke Zhou¹⁶, Wanjin Lu^{1,2}, Jintao Xie¹⁷, Jianhua Fang¹⁶, Jinhuang Cao^{1,2},
 Chen-Chen Miao¹⁸, Yuhao Zhu^{1,2}, Yunchuan Chen¹⁶, Xiaofeng Cheng¹⁶, Yinan Ke¹⁶,
 Yong-Kun Zhang¹, Long-Xuan Zhang¹⁵, Shuo Cao^{12,2}, Shiyan Tian¹⁵, Zi-Wei Wu¹,
 Chunfeng Zhang¹, Jiarui Niu¹, Dejiang Zhou¹, Silu Xu^{1,2}, Bojun Wang¹,
 Huaxi Chen¹⁶, Xiang-Lei Chen¹, Xianghan Cui¹, Yi Feng^{16,19},
 Erbil Gügercinoğlu^{1,20}, Yu-Xiang Huang^{12,2}, Jian Li^{21,22}, Dongming Li³,
 Dong-Zi Li²³, Ye Li²⁴, Lin Lin^{3,4}, Xiaohui Liu^{1,2}, Rui Luo²⁵, Jia-Wei Luo^{26,27},
 Chen-Hui Niu²⁸, Qingyue Qu^{1,2}, Yuanhong Qu^{9,10}, Habtamu Menberu Tedila¹,
 Chengjie Wang³⁰, Wei-Yang Wang², Yabiao Wang³⁰, Yi-Dan Wang^{1,2},
 Suming Weng^{31,32}, Yunsheng Wu³⁰, Heng Xu¹, Aiyuan Yang^{1,5}, Yuan-Pei Yang³³,
 Shihan Yew^{31,32}, Wenfei Yu³⁴, Lei Zhang^{1,35}, Rushuang Zhao³⁶

¹National Astronomical Observatories, Chinese Academy of Sciences, Beijing 100101, China

²University of Chinese Academy of Sciences, Beijing 100049, China

³School of Physics and Astronomy, Beijing Normal University, Beijing 100875, China

⁴Institute for Frontiers in Astronomy and Astrophysics, Beijing Normal University, Beijing 102206, China

⁵State Key Laboratory of Radio Astronomy and Technology, Beijing 100101, China

- ⁶School of Astronomy and Space Science, Nanjing University, Nanjing 210023, China
- ⁷New Cornerstone Science Laboratory, Department of Astronomy, Tsinghua University, Beijing 100084, China
- ⁸Department of Physics, University of Hong Kong, Pokfulam Road, Hong Kong, China
- ⁹Nevada Center for Astrophysics, University of Nevada, Las Vegas, NV 89154, USA
- ¹⁰Department of Physics and Astronomy, University of Nevada Las Vegas, Las Vegas, NV 89154, USA
- ¹¹Department of Astronomy, Peking University, Beijing 100871, China
- ¹²Yunnan Astronomical Observatories, Chinese Academy of Sciences, Kunming 650216, Yunnan, China
- ¹³Beijing Laser Acceleration Innovation Center, Huairou, Beijing 101400, China
- ¹⁴Key Laboratory of Modern Astronomy and Astrophysics (Nanjing University), Ministry of Education, Nanjing 210023, China
- ¹⁵School of Physics, Huazhong University of Science and Technology, Wuhan 430074, China
- ¹⁶Research Center for Astronomical Computing, Zhejiang Laboratory, Hangzhou 311100, China
- ¹⁷School of Computer Science and Engineering, Sichuan University of Science and Engineering, Yibin 644000, China
- ¹⁸College of Physics and Electronic Engineering, Qilu Normal University, Jinan 250200, China
- ¹⁹Institute for Astronomy, School of Physics, Zhejiang University, Hangzhou 310027, China
- ²⁰School of Arts and Science, Qingdao Binhai University, Qingdao 266525, China
- ²¹Department of Astronomy, School of Physical Sciences, University of Science and Technology of China, Hefei 230026, China
- ²²School of Astronomy and Space Science, University of Science and Technology of China, Hefei 230026, China
- ²³Department of Astronomy, Tsinghua University, Beijing 100084, China
- ²⁴Purple Mountain Observatory, Chinese Academy of Sciences, Nanjing 210023, China
- ²⁵Department of Astronomy, School of Physics and Materials Science, Guangzhou University, Guangzhou, China
- ²⁶College of Physics and Hebei Key Laboratory of Photophysics Research and Application, Hebei Normal University, Shijiazhuang, Hebei 050024, China
- ²⁷Shijiazhuang Key Laboratory of Astronomy and Space Science, Hebei Normal University, Shijiazhuang, Hebei 050024, China
- ²⁸Institute of Astrophysics, Central China Normal University, Wuhan 430079, China
- ²⁹Department of Physics and Astronomy, University of Nevada, Las Vegas 89154, USA
- ³⁰Tencent Youtu Lab, Shanghai 200030, China

³¹National Key Laboratory of Dark Matter Physics, School of Physics and Astronomy, Shanghai Jiao Tong University, Shanghai 200240, China

³²Laboratory for Laser Plasmas and Collaborative Innovation Centre of IFSA, Shanghai Jiao Tong University, Shanghai 200240, China

³³South-Western Institute for Astronomy Research, Key Laboratory of Survey Science of Yunnan Province, Yunnan University, Kunming, Yunnan 650500, China

³⁴Shanghai Astronomical Observatory, Chinese Academy of Sciences, Shanghai 200030, China

³⁵Centre for Astrophysics and Supercomputing, Swinburne University of Technology, Hawthorn 3122, Australia

³⁶Guizhou Normal University, Guizhou Provincial Key Laboratory of Radio Astronomy and Data Processing, Guiyang 550001, China

*Corresponding author. Email: wangpei@nao.cas.cn; gaohe@bnu.edu.cn; dili@tsinghua.edu.cn; zhuww@nao.cas.cn; bzhang1@hku.hk

†These authors contributed equally to this work.

Magnetars are widely considered to be the central engine of fast radio bursts (FRBs), capable of driving coherent radio emission through magnetic energy release. The accumulation of burst energy can be employed as a probe to reveal the nature of FRB energy engine. Current observations of repeaters have not yet provided sufficient constraints on the magnetic energy budget for magnetar models. Here we report 11,553 bursts detected from the hyper-active repeating source FRB 20240114A over 214 days during a recent active episode, with a peak burst rate as high as 729 hr^{-1} , above the detection threshold of the monitoring observations using Five-hundred-meter Aperture Spherical radio Telescope (FAST). This represents the largest recorded burst sample from a single FRB source, comprising more than four times as many bursts as any previously known repeater and exceeding the cumulative total of all published bursts to date. Assuming a typical value of radio efficiency of 10^{-4} and a beaming factor of 0.1, the estimated total isotropic burst energy of this source exceeds 86% of the dipolar magnetic energy of a typical magnetar with a polar surface magnetic field of 10^{15} G and a radius of 10^6 cm . The total energy release of this source is about one and a half orders of magnitude higher than that of other known repeaters. We further provide the most stringent lower limit of $4.7 \times 10^{32} \text{ G cm}^3$ on the magnetic moment of the underlying magnetar. The findings suggest that either the central engine emits

with exceptionally high radio efficiency, possesses a small beaming factor, or it should be a more powerful compact object than typically considered in current magnetar models.

INTRODUCTIONS

Fast radio bursts (FRBs) are bright, millisecond duration radio transients occurring at cosmological distances (1–3). Although their origins and emission mechanisms remain highly uncertain, FRB pulses bear similarities to Galactic magnetar signals (4, 5), suggesting a latent magnetar origin. Two main categories of magnetar models have been proposed: one involving emission from within the magnetosphere (6–8), and another from relativistic shocks outside the light cylinder (9, 10). Recent observations of polarization and scintillation properties favor the magnetospheric models (11–15). Some FRB sources have been observed to repeat, with some exhibiting high activity and producing up to thousands of pulses (16–20). These prolific repeaters require an active central engine and a substantial energy reservoir, thus providing important clues to re-evaluate the adequacy of the energy budget for magnetar models.

OBSERVATIONS

In response to alerts from the Virtual Observatory Event (VOEvent) Service of the Canadian Hydrogen Intensity Mapping Experiment Fast Radio Burst project (CHIME/FRB VOEvent) (21), we conducted extensive L-band (1-1.5 GHz) observations of the hyper-active repeating FRB 20240114A using the Five-hundred-meter Aperture Spherical radio Telescope (FAST). Our observations spanned from 28 January 2024 to 29 August 2024 (UT), accumulating a total exposure time of 33.86 hours.

During the 214-day observation campaign, we detected a total of 11,553 independent bursts above the 0.026 Jy ms ($\sim 12\sigma$) fluence detection threshold of FAST. The daily observations and the burst statistics are illustrated in Fig.1. Panel A shows the observation sessions and cumulative burst counts, while Panel C displays the average burst rates on each day. The source exhibited continuous activity throughout the observation campaign, demonstrating a variable burst rate ranging from 4 hr^{-1} to 729 hr^{-1} and a mean rate of 249 hr^{-1} . Notably, during six observing sessions, the burst rate

exceeded 542 hr^{-1} , surpassing the highest previously reported rate for FRB 20201124A (19). These observations confirm FRB 20240114A as an exceptionally hyper-active and long-lived repeating source. The burst rate demonstrated two distinct episodes, with a peak of 729 hr^{-1} on 12 March, followed by a secondary peak of 416 hr^{-1} on 28 July 2024 (UT). The temporal patterns are visualized in the energy-epoch kernel density estimation (KDE) color map (Fig. 1B).

RESULTS

We measured the peak flux density, pulse width, bandwidth, central frequency, fluence, and isotropic equivalent energy of each burst. The structure-optimized observational dispersion measure (DM) (22, 23) was also determined, yielding a median value of 529.1 pc cm^{-3} with a standard deviation of 1.3 pc cm^{-3} . No significant trend was observed in the temporal evolution of the median value of these parameters. We carried out a comprehensive correlation analysis among the measured parameter pairs of the bursts. The Pearson correlation coefficient (PCC) indicates an absence of significant correlation between the parameter pairs, except for those that are inherently interdependent (see details in Materials and Methods). We tested whether high burst rates could cause systematic feedback on the FRB and its propagation properties, as high radiation pressure may affect the surrounding environment (24). No correlation was found between these observational parameters and the burst rate (see details in Materials and Methods). This result suggests that frequent triggering of the bursts has no significant impact on the circumburst environment and the radiation mechanism.

The waiting time between two adjacent bursts is calculated for bursts within the same observing session to avoid long gaps. Each pulse time of arrival (ToA) was transformed to the Solar System barycentre in barycentric coordinate time (TCB). The waiting time distribution exhibits a prominent bimodal characteristic with two distinct time scales, featuring peaks centred at approximately 7.11 seconds and 34 milliseconds. Each peak is well described by a log-normal distribution. We further compared the waiting time peaks with other known repeating FRB sources. We observed a similarity in the left peaks, which may reveal intrinsic burst-to-burst properties shared by FRB sources, while the right peaks of the waiting time distribution represent the activity level of the FRB source during the observation campaign (see details in Materials and Methods).

The large burst sample from FRB 20240114A allows us to update constraints on the average

luminosity and the total energy budget of FRB sources. The total isotropic equivalent energy of this source is estimated to be $E_{\text{src}} = (1.47 \times 10^{47} \text{ erg}) F_{\text{b},-1} \eta_{\text{r},-4}^{-1} (\zeta/0.0066)^{-1}$ during the FAST observation campaign. Here, $\eta_{\text{r},-4}$ denotes the radio efficiency in units of 10^{-4} . A typical value of 10^{-4} is adopted, based on the observational upper limit of $\eta_{\text{r}} = 10^{-4} - 10^{-5}$ inferred from the peculiar event FRB 20200428D, which was associated with X-ray bursts (25, 26). The global beaming factor $F_{\text{b}} = 0.1 F_{\text{b},-1}$ is introduced because the bursts may be confined to a global fan beam, so that the net energy is smaller than the estimated isotropic equivalent value (27). The duty cycle scaling factor ζ represents the ratio of the total observation time to the full time span of the campaign, which is used to account for the emission energy of FRB 20240114A during unobserved periods. Compared with the total dipolar magnetic energy of a typical magnetar with a polar surface magnetic field $B_p = 10^{15}$ G and radius $R = 10^6$ cm, which corresponds to $E_{\text{mag}} = (1/6) B_p^2 R^3 \simeq (1.7 \times 10^{47} \text{ erg}) B_{p,15}^2 R_6^3$, the burst energy E_{src} already exceeds $86\% F_{\text{b},-1} \eta_{\text{r},-4}^{-1} (\zeta/0.0066)^{-1} B_{p,15}^{-2} R_6^{-3}$ of the available magnetar energy during the 214-day observation campaign.

We further provide a stringent constraint on the magnetic moment of the central magnetar as $\mu = (1/2) B_p R^3 > 4.7 \times 10^{32} F_{\text{b},-1}^{1/2} \eta_{\text{r},-4}^{-1/2} (\zeta/0.0066)^{1/2} R_6^{3/2} \text{ G cm}^3$, which corresponds to a magnetic field of $B_p > 9.4 \times 10^{14} F_{\text{b},-1}^{1/2} \eta_{\text{r},-4}^{-1/2} (\zeta/0.0066) R_6^{-3/2} \text{ G}$. Fig. 2 illustrates the fraction of the total estimated E_{src} relative to the available magnetar energy, and the lower limit of the central magnetar's magnetic moment for this source and other repeaters (16–20). The total energy of this source exceeds that of other active repeaters by more than a factor of 30, approaching the typical magnetic energy of a single magnetar. This result imposes the most stringent constraint to date on the FRB central engine model from an energy budget perspective.

The burst rate distribution of energy for FRB 20240114A (Fig. 3A) shows a characteristic energy E_c around 1×10^{37} erg with a high-energy tail. The distribution cannot be well fitted as a whole with a single power-law function simultaneously in the energy regions below and above E_c . Power-law fits applied separately above different energy thresholds yield non-converging indices (Fig. 3C). This indicates that a power-law function does not adequately describe the distribution, even above the characteristic energy. We then modeled the distribution using single and bimodal log-normal functions. The single log-normal model shows significant systematic deviations in both the low- and high-energy regions (Fig. 3B, D). Statistical metrics (\bar{R}^2 , reduced χ^2 , AIC) confirm that the bimodal function fits better represent the data (see details in Materials and Methods). This

complex bimodal distribution suggests the presence of diverse burst types, indicating multiple burst populations or distinct emission mechanisms in repeating FRBs (3).

DISCUSSION

The extreme and continuous activity of this prolific source indicates a substantial energy emission and frequent triggering, leading to a crisis of at least some magnetar models. As the total energy release of this source is approaching the typical magnetic energy of a single magnetar, models that invoke a large global beaming factor and low radiation efficiency face significant challenges in light of these observations. In particular, the synchrotron maser shock model (9, 10), which typically predicts a low radio efficiency and a wide beaming angle, is strongly disfavored. The magnetospheric models (6–8), which invoke narrow emission beams and flexible radio efficiencies (28–30), may still be possible, even though contrived conditions are required to satisfy observational constraints. The extremely high event rate also poses a challenge to the FRB triggering mechanism. Starquakes, which are considered the leading trigger scenario for FRBs, may still be able to account for the observed average burst rate (249 hr^{-1}) during our 214-day observation campaign, according to the estimation in Ref. (31). The high event rates may also cause distortions in the magnetic field lines, thus challenging the possibility of generating coherent emission at millisecond-level waiting timescales based on our observations.

A continuous monitoring of FRB 20240114A in the future may help further constrain the nature of the central engine. Given the persistent and highly active behavior exhibited by FRB 20240114A over data spanning more than 8 months, the central engine of this source should be characterized by either an exceptionally high radio emission efficiency, a small beaming factor, or a much energetic compact object than is conventionally anticipated in prevailing isolated magnetar models.

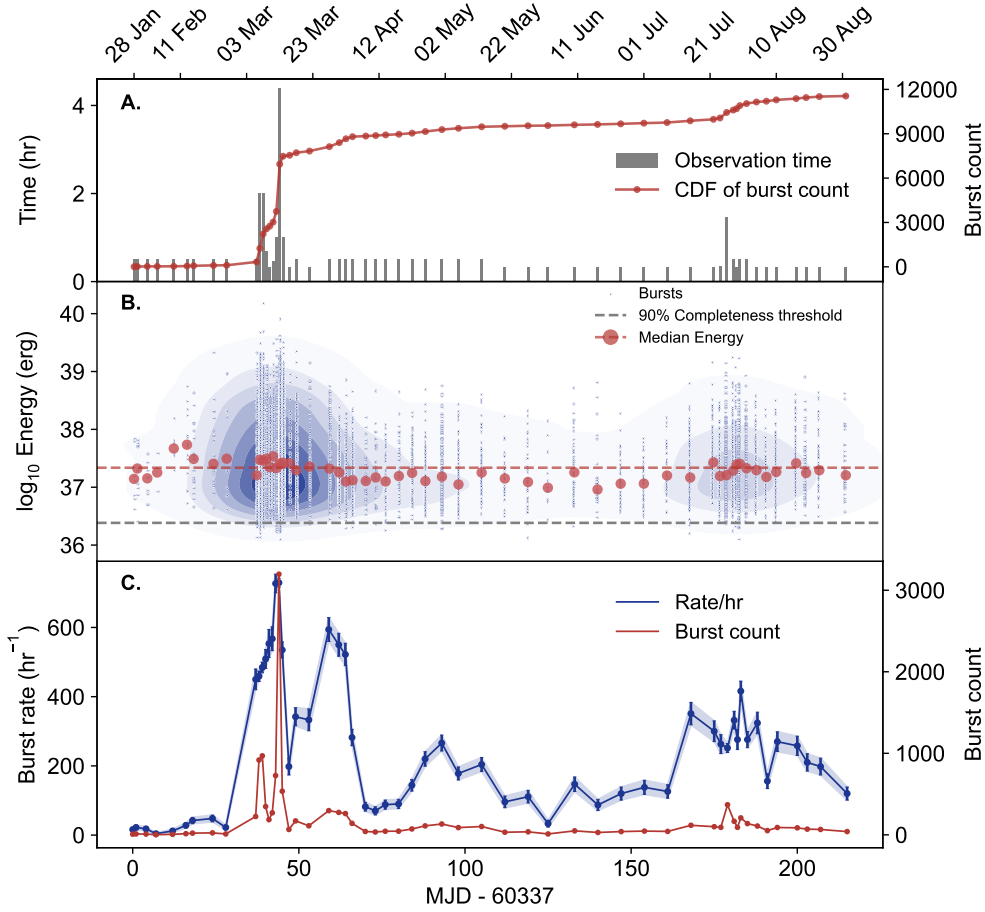


Figure 1: The time-dependent energy distribution and detection of the bursts from FRB 20240114A during the observation campaign. Panel A: The length of each observation session is represented by the grey bar, while the cumulative number distribution of the bursts is indicated by the red solid line with dots. Panel B: Time-dependent burst energy distribution. The blue dots indicate the bursts, while the red dots represent the daily median energy value. The red dashed line shows the median value of all the bursts. The grey dashed line indicates the 90% detection completeness threshold of FAST (0.023 Jy ms for an assumed pulse width of 3 ms (*16*)). The blue contour is the 2D kernel density estimation (KDE) of the isotropic burst energies. Panel C: The red colouration denotes the burst counts, and the blue colouration denotes the burst rates with Poisson counting errors, for each observation day.

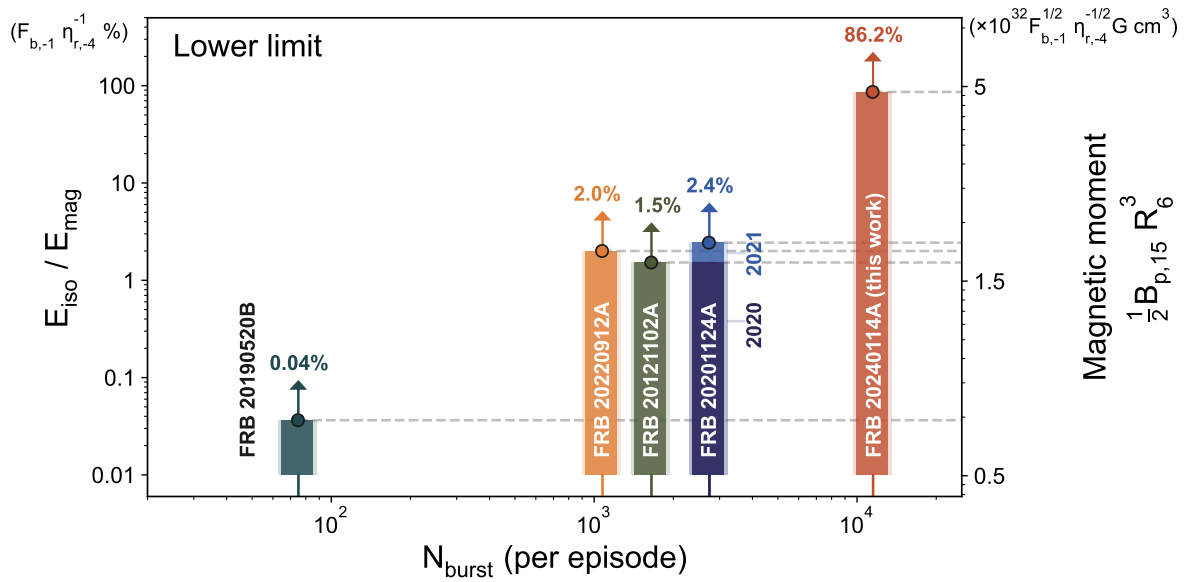


Figure 2: The isotropic energy fraction and magnetic moment of FRBs. The plot presents the isotropic energy fraction ($E_{\text{iso}}/E_{\text{mag}}$) versus the burst number per episode (N_{burst}) for active repeaters. The percentages indicated on the bars represent the corresponding isotropic energy fraction for each FRB source. The lower limit on the magnetic moment of the central magnetar is shown on the right axis.

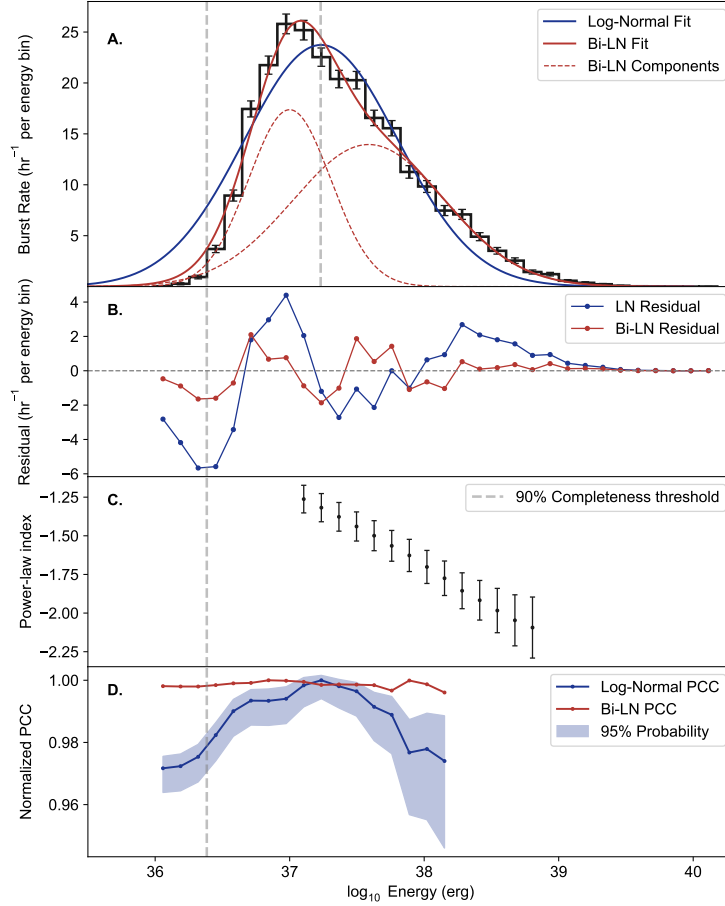


Figure 3: Burst rate distribution of the isotropic equivalent energy for bursts from FRB 20240114A. The 90% detection completeness threshold is shown by the vertical gray dashed line. Panel A: Burst rate distribution of energy. The blue solid line shows represents the best-fit single log-normal model of the distribution. The red solid line indicates the optimal bimodal fit, with its individual components delineated as red dashed lines. Panel B: The residuals of the single log-normal function and bimodal fits to the burst rate distribution. The blue line corresponds to the residuals from the single log-normal function fit, while the red line shows the residuals from the bimodal fit. Panel C: The spectral index of single power-law fitting as a function of the energy threshold. Panel D: The normalized Pearson Correlation Coefficient (PCC) as a function of the energy threshold. The blue solid line denotes the results of the log-normal (single log-normal function) fit, and the blue shaded region represents the 95% probability interval of the normalized PCC. The red solid line indicates the normalized PCC obtained from a bimodal fit using two log-normal components.

References and Notes

1. D. R. Lorimer, M. Bailes, M. A. McLaughlin, D. J. Narkevic, F. Crawford, A Bright Millisecond Radio Burst of Extragalactic Origin. *Science* **318** (5851), 777–780 (2007), doi:10.1126/science.1147532.
2. M. Bailes, The Discovery and Scientific Potential of Fast Radio Bursts. *Science* **378** (6620), eabj3043 (2022), doi:10.1126/science.abj3043.
3. E. Petroff, J. W. T. Hessels, D. R. Lorimer, Fast Radio Bursts at the Dawn of the 2020s. *The Astronomy and Astrophysics Review* **30** (1), 2 (2022), doi:10.1007/s00159-022-00139-w.
4. C. D. Bochenek, *et al.*, A Fast Radio Burst Associated with a Galactic Magnetar. *Nature* **587** (7832), 59–62 (2020), doi:10.1038/s41586-020-2872-x.
5. The CHIME/FRB Collaboration, *et al.*, A Bright Millisecond-Duration Radio Burst from a Galactic Magnetar. *Nature* **587** (7832), 54–58 (2020), doi:10.1038/s41586-020-2863-y.
6. P. Kumar, W. Lu, M. Bhattacharya, Fast Radio Burst Source Properties and Curvature Radiation Model. *Monthly Notices of the Royal Astronomical Society* **468** (3), 2726–2739 (2017), doi:10.1093/mnras/stx665.
7. W. Lu, P. Kumar, B. Zhang, A Unified Picture of Galactic and Cosmological Fast Radio Bursts. *Monthly Notices of the Royal Astronomical Society* **498** (1), 1397–1405 (2020), doi:10.1093/mnras/staa2450.
8. Y.-P. Yang, B. Zhang, Fast Radio Bursts and Their High-energy Counterparts from Magnetar Magnetospheres. *The Astrophysical Journal* **919** (2), 89 (2021), doi:10.3847/1538-4357/ac14b5.
9. B. D. Metzger, B. Margalit, L. Sironi, Fast Radio Bursts as Synchrotron Maser Emission from Decelerating Relativistic Blast Waves. *Monthly Notices of the Royal Astronomical Society* **485** (3), 4091–4106 (2019), doi:10.1093/mnras/stz700.

10. B. Margalit, B. D. Metzger, L. Sironi, Constraints on the Engines of Fast Radio Bursts. *Monthly Notices of the Royal Astronomical Society* **494** (4), 4627–4644 (2020), doi:10.1093/mnras/staa1036.
11. R. Luo, *et al.*, Diverse Polarization Angle Swings from a Repeating Fast Radio Burst Source. *Nature* **586** (7831), 693–696 (2020), doi:10.1038/s41586-020-2827-2.
12. J. R. Niu, *et al.*, Sudden Polarization Angle Jumps of the Repeating Fast Radio Burst FRB 20201124A. *The Astrophysical Journal Letters* **972** (2), L20 (2024), doi:10.3847/2041-8213/ad7023.
13. R. Mckinven, *et al.*, A Pulsar-like Polarization Angle Swing from a Nearby Fast Radio Burst. *Nature* **637** (8044), 43–47 (2025), doi:10.1038/s41586-024-08184-4.
14. K. Nimmo, *et al.*, Magnetospheric Origin of a Fast Radio Burst Constrained Using Scintillation. *Nature* **637** (8044), 48–51 (2025), doi:10.1038/s41586-024-08297-w.
15. J. Jiang, *et al.*, Ninety percent circular polarization detected in a repeating fast radio burst. *National Science Review* **12** (2), nwae293 (2024), doi:10.1093/nsr/nwae293.
16. D. Li, *et al.*, A Bimodal Burst Energy Distribution of a Repeating Fast Radio Burst Source. *Nature* **598** (7880), 267–271 (2021), doi:10.1038/s41586-021-03878-5.
17. C.-H. Niu, *et al.*, A Repeating Fast Radio Burst Associated with a Persistent Radio Source. *Nature* **606** (7916), 873–877 (2022), doi:10.1038/s41586-022-04755-5.
18. H. Xu, *et al.*, A Fast Radio Burst Source at a Complex Magnetized Site in a Barred Galaxy. *Nature* **609** (7928), 685–688 (2022), doi:10.1038/s41586-022-05071-8.
19. Y.-K. Zhang, *et al.*, FAST Observations of an Extremely Active Episode of FRB 20201124A. II. Energy Distribution. *Research in Astronomy and Astrophysics* **22** (12), 124002 (2022), doi:10.1088/1674-4527/ac98f7.
20. Y.-K. Zhang, *et al.*, FAST Observations of FRB 20220912A: Burst Properties and Polarization Characteristics. *The Astrophysical Journal* **955** (2), 142 (2023), doi:10.3847/1538-4357/aced0b.

21. T. C. Abbott, *et al.*, Frb-Voe: A Real-time Virtual Observatory Event Alert Service for Fast Radio Bursts. *The Astronomical Journal* **169** (1), 39 (2025), doi:10.3847/1538-3881/ad9451.
22. K. Nimmo, *et al.*, Highly Polarized Microstructure from the Repeating FRB 20180916B. *Nature Astronomy* **5** (6), 594–603 (2021), doi:10.1038/s41550-021-01321-3.
23. H.-H. Lin, *et al.*, DM-power: An Algorithm for High Precision Dispersion Measure with Application to Fast Radio Bursts (2023), <http://arxiv.org/abs/2208.13677>.
24. W. Lu, E. S. Phinney, Imprint of Local Environment on Fast Radio Burst Observations. *Monthly Notices of the Royal Astronomical Society* **496** (3), 3308–3313 (2020), doi:10.1093/mnras/staa1679.
25. S. Mereghetti, *et al.*, INTEGRAL Discovery of a Burst with Associated Radio Emission from the Magnetar SGR 1935+2154. *The Astrophysical Journal Letters* **898** (2), L29 (2020), doi:10.3847/2041-8213/aba2cf.
26. C. K. Li, *et al.*, HXMT Identification of a Non-Thermal X-ray Burst from SGR J1935+2154 and with FRB 200428. *Nature Astronomy* **5** (4), 378–384 (2021), doi:10.1038/s41550-021-01302-6.
27. B. Zhang, The Physics of Fast Radio Bursts. *Reviews of Modern Physics* **95** (3), 035005 (2023), doi:10.1103/RevModPhys.95.035005.
28. A. Szary, B. Zhang, G. I. Melikidze, J. Gil, R.-X. Xu, RADIO EFFICIENCY OF PULSARS. *The Astrophysical Journal* **784** (1), 59 (2014), doi:10.1088/0004-637x/784/1/59.
29. A. M. Cook, *et al.*, Contemporaneous X-Ray Observations of 30 Bright Radio Bursts from the Prolific Fast Radio Burst Source FRB 20220912A. *The Astrophysical Journal* **974** (2), 170 (2024), doi:10.3847/1538-4357/ad6a13.
30. Y. Qu, B. Zhang, Coherent Inverse Compton Scattering in Fast Radio Bursts Revisited. *The Astrophysical Journal* **972** (1), 124 (2024), doi:10.3847/1538-4357/ad5d5b.

31. W.-Y. Wang, *et al.*, On the Energy Budget of Starquake-induced Repeating Fast Radio Bursts. *Research in Astronomy and Astrophysics* **24** (10), 105012 (2024), doi:10.1088/1674-4527/ad74db.
32. K. Shin, *et al.*, The CHIME/FRB Discovery of the Extremely Active Fast Radio Burst Source FRB 20240114A (2025), doi:10.48550/arXiv.2505.13297.
33. J. Tian, *et al.*, Detection and Localization of the Highly Active FRB 20240114A with MeerKAT. *Monthly Notices of the Royal Astronomical Society* **533** (3), 3174–3193 (2024), doi:10.1093/mnras/stae2013.
34. R. Nan, *et al.*, THE FIVE-HUNDRED-METER APERTURE SPHERICAL RADIO TELESCOPE (FAST) PROJECT. *International Journal of Modern Physics D* **20** (06), 989–1024 (2011).
35. D. Li, *et al.*, FAST in Space: Considerations for a Multibeam, Multipurpose Survey Using China’s 500-m Aperture Spherical Radio Telescope (FAST). *IEEE Microwave Magazine* **19** (3), 112–119 (2018), doi:10.1109/MMM.2018.2802178.
36. D. Li, *et al.*, Decadal Evolution of a Repeating Fast Radio Burst Source (2025), doi:10.21203/rs.3.rs-5854536/v1.
37. S. M. Ransom, *New Search Techniques for Binary Pulsars*, Ph.D. thesis, Harvard University, Massachusetts (2001).
38. Y.-K. Zhang, *et al.*, DRAFTS: A Deep-learning-based Radio Fast Transient Search Pipeline. *The Astrophysical Journal Supplement Series* **276** (1), 20 (2025), doi:10.3847/1538-4365/ad8f31.
39. P. Wang, *et al.*, X-Ray Hardening Preceding the Onset of SGR 1935+2154’s Radio Pulsar Phase. *The Astrophysical Journal Supplement Series* **275** (2), 39 (2024), doi:10.3847/1538-4365/ad7c3f.
40. J.-T. Xie, *et al.*, Polarization Characteristics of the Hyperactive FRB 20240114A. *The Astrophysical Journal Supplement Series* **278** (2), 49 (2025), doi:10.3847/1538-4365/add2eb.

41. C.-R. Hu, *et al.*, Decoding FRB energetics and frequency features hidden by observational incompleteness. *arXiv e-prints* arXiv:2503.18084 (2025), doi:10.48550/arXiv.2503.18084.
42. P. Jiang, *et al.*, The Fundamental Performance of FAST with 19-Beam Receiver at L Band. *Research in Astronomy and Astrophysics* **20** (5), 064 (2020), doi:10.1088/1674-4527/20/5/64.
43. X. Zhang, W. Yu, Z. Yan, Y. Xing, B. Zhang, A Flaring Radio Counterpart to a Fast Radio Burst Reveals a Newborn Magnetized Engine (2025), doi:10.48550/arXiv.2501.14247.
44. B. Zhang, Fast Radio Burst Energetics and Detectability from High Redshifts. *The Astrophysical Journal Letters* **867** (2), L21 (2018), doi:10.3847/2041-8213/aae8e3.
45. K. Gourdji, *et al.*, A Sample of Low-energy Bursts from FRB 121102. *The Astrophysical Journal Letters* **877** (2), L19 (2019), doi:10.3847/2041-8213/ab1f8a.
46. Planck Collaboration, *et al.*, Planck2015 Results: XIII. Cosmological Parameters. *Astronomy & Astrophysics* **594**, A13 (2016), doi:10.1051/0004-6361/201525830.
47. X.-L. Chen, *et al.*, The Host Galaxy of the Hyperactive Repeating FRB 20240114A: Behind a Galaxy Cluster. *The Astrophysical Journal Letters* **980** (2), L24 (2025), doi:10.3847/2041-8213/adadfd.
48. K. P. Burnham, D. R. Anderson, K. P. Burnham, *Model Selection and Multimodel Inference: A Practical Information-Theoretic Approach* (Springer, New York), 2nd ed ed. (2002).
49. Y.-X. Huang, *et al.*, The Flat Tail in the Burst Energy Distribution of FRB 20240114A. *Research in Astronomy and Astrophysics* **25** (8), 085009 (2025), doi:10.1088/1674-4527/ade34e.
50. G. B. Hobbs, R. T. Edwards, R. N. Manchester, Tempo2, a New Pulsar-Timing Package - I. An Overview: Tempo2, a New Pulsar-Timing Package - I. Overview. *Monthly Notices of the Royal Astronomical Society* **369** (2), 655–672 (2006), doi:10.1111/j.1365-2966.2006.10302.x.
51. J.-W. Luo, *et al.*, Hyper-Active Repeating Fast Radio Bursts from Rotation Modulated Starquakes on Magnetars (2025), doi:10.48550/arXiv.2502.16626.

Acknowledgments

This work made use of data from FAST, a Chinese national mega-science facility built and operated by the National Astronomical Observatories, Chinese Academy of Sciences. This work made use of the data from FAST FRB Key Science Project. This research made use of the CHIME/FRB VOEvent Service, BlinkVerse and TransientVerse.

Funding: This work is supported by National Natural Science Foundation of China (NSFC) Programs Nos. 12588202, 11690024, 11725313, 11988101, 12041303, 12041306, 12203045, 12233002, 12303042, 12403100, 12421003, 12447115, U1731238, U2031117, W2442001; the CAS International Partnership Program No. 114-A11KYSB20160008; the CAS Strategic Priority Research Program No. XDB23000000; the National Key R&D Program of China (Nos. 2017YFA0402600, 021YFA0718500) and the National SKA Program of China (Nos. 2020SKA0120200, 2020SKA0120300, 2022SKA0130104). P.W. acknowledges support from the CAS Youth Interdisciplinary Team, the Youth Innovation Promotion Association CAS (id. 2021055), and the Cultivation Project for FAST Scientific Payoff and Research Achievement of CAMS-CAS. Q.W. is supported by the China Postdoctoral Science Foundation (CPSF) under Grant Nos. GZB20240308, 2025T180875, 2025T180875. D.L. is a New Cornerstone investigator. W.W.Z. is supported by the CAS Project for Young Scientists in Basic Research, YSBR-063. Y.F.H. acknowledges the support from the Xinjiang Tianchi Program. Y.F. is supported by the Leading Innovation and Entrepreneurship Team of Zhejiang Province of China grant No. 2023R01008, and by Key R&D Program of Zhejiang grant No. 2024SSYS0012.

Author contributions: J.S.Z. and T.C.W. led the FAST data analysis. P.W., H.G., D.L., B.Z. and W.W.Z. are the conveners of the project, coordinated the science team, and launched the FAST observational campaign on FRB 20240114A. Q.W., D.K.Z., W.J.L., J.T.X., J.H.F., J.H.C., C.C.M., Y.H.Z., Y.C.C., X.F.C., Y.N.K., Y.K.Z., Y.F., S.C., S.Y.T., L.X.Z., Z.W.W., C.F.Z., J.R.N., D.J.Z., S.L.X., B.J.W. participated in the FAST data analysis. B.Z. and Y.P.Y. led the theoretical interpretation. J.S.Z., P.W. and D.L. contributed to the writing of the manuscript. All authors discussed the contents and form the final version of the paper.

Competing interests: There are no competing interests to declare.

Data and materials availability: Observational properties of 11,553 burst events of FRB 20240114A measured with FAST from January 2024 to August 2024 are summarized in the manuscript Supplementary Table S2 and <https://doi.org/10.57760/sciencedb.Fastro.00030>. Raw data are available from the FAST archive: <https://fast.bao.ac.cn>. Due to the large data volume for these observations, interested users are encouraged to contact the corresponding author to arrange the data transfer. All data needed to evaluate the conclusions in the paper are present in the paper and/or the Supplementary Materials.

Computational programs for the FRB 20240114A burst analysis and observations reported here are available at <https://github.com/NAOC-pulsar/PeiWang-code>. Other standard data reduction packages are available at their respective websites:

PRESTO: <https://github.com/scottransom/presto>

DRAFTS: <https://github.com/SukiYume/DRAFTS>

DSPSR: <https://dspsr.sourceforge.net>

PSRCHIVE: <https://psrchive.sourceforge.net>

DM-power: <https://github.com/hsiuhsil/DM-power>

Supplementary materials

Materials and Methods

Figs. S1 to S3

Tables S1 to S4

References

Supplementary Materials for

A prolific repeating fast radio burst source and a crisis of the magnetar model

Jun-Shuo Zhang[†], Tian-Cong Wang[†], et al.

*Corresponding authors: Pei Wang, He Gao, Di Li, Wei-Wei Zhu, Bing Zhang. Email: wangpei@nao.cas.cn; gaohe@bnu.edu.cn; dili@tsinghua.edu.cn; zhuww@nao.cas.cn; bzhang1@hku.hk

[†]These authors contributed equally to this work.

This PDF file includes:

Materials and Methods

Supplementary Text

Figures S1 to S3

Tables S1 to S4

Materials and Methods

Observation Campaign and Data Reduction

FAST monitored the repeating FRB 20240114A continuously from 2024 January 28 to 2024 August 29 (UT), using the central beam of 19-beam L-band receiver, initially pointing to the coordinate of RA= $21^h27^m39^s.888$, Dec= $+04^\circ21'0''.36$ as reported by CHIME (32). We then calibrated the pointing to the position of RA= $21^h27^m39^s.84$, Dec= $+04^\circ19'46''.3$ localized by MeerKAT (33) starting from 2024 February 15 (UT). During the observation campaign, 57 observation sessions with a total of 33.86 hours exposure time were conducted. The FAST 19-beam L-band receiver covers a frequency bandwidth of 1.0-1.5 GHz (34, 35). Most of the data were recorded in 8-bit PSRFIT format over 4096 frequency channels with a time resolution of $49.152 \mu\text{s}$, while some were recorded with different parameters (see Supplementary Table S1).

We performed the same dedicated single-pulse search described in Ref. (36), using the PRESTO software (37). We created the de-dispersed time series for each pseudo-pointing over a range of DMs of 515-540 pc cm^{-3} , and also applied a zero-DM matched filter to mitigate radio frequency interference (RFI) in blind-search. All the potential candidate plots were subsequently inspected visually.

We also employed the improved deep learning-based search tool DRAFTS (38) and the AI-aided data filtering pipeline described in Ref. (39) to cross-verify the search results. Then, we used the equivalent burst duration W_{eq} of each burst, which was computed by dividing the fluence by the peak flux, to refine the detected fluence signal-to-noise ratio (SNR_f , corresponding to integrated flux and the burst energy).

A total of 11,553 bursts were detected during the observation campaign above our detection threshold $\text{SNR}_f > 12$ (see Supplementary Table S2 for the full catalog).

The FAST receiver experiences saturation when the radio flux density reaches levels ranging from hundreds of Jansky to mega-Jansky. To identify potential saturation events in the recorded data streams, we examined all Stokes components in epochs where 50% of the frequency channels met one of the following conditions: a) the channel is fully saturated (255 value in 8-bit channels), b) the channel is zero-valued, c) the Root Mean Square (RMS) of the bandpass is less than 2. We identified saturation events in our observations conducted from March 8 to 10. Data affected by

saturation during these periods were excluded from further analysis.

Since FAST records data in 8-bit format, saturation also occurs when pulse brightness exceeds the dynamic range limit of 255, leading to an underestimation of flux. Pulses affected by saturation and potential flux underestimation were marked in the Supplementary Table S2.

Burst Characterization and Calibration

We refined the measurement of DM value for each burst using the ‘DM-power’ package, which employs an algorithm that optimally weights the pulse structure at each Fourier frequency (23). For bursts with obscured morphological structures in the time-frequency dynamic spectrum or those with low SNR, the DM-power package may introduce overfitting artifacts. In such cases, we utilized the daily average DM values instead. The median value of the DM is 529.1 pc cm^{-3} with a standard deviation of 1.3 pc cm^{-3} , which is consistent with the CHIME’s measurement (32).

The frequency boundaries of the bursts were calculated using a systematically adjusted method based on the behavior of the first derivative of the cumulative distribution function (CDF) of the spectrum (40). For bursts truncated by the upper or lower limits of the observed frequency range, a frequency-extended Gaussian fit was applied to correct the bandwidth (41). In cases where the bursts showed complex morphological structures or were too faint to yield a reliable result, a boxcar bandwidth was adopted instead.

We injected a 10 K equivalent noise calibration before each session, which was used to scale the data to T_{sys} units. The frequency-averaged specific peak flux density S_ν within the frequency boundaries for each burst was calibrated against the baseline noise level, and then measured for the amount of pulsed flux density above the baseline. The temporal variation of the background was reconstructed by the telescopic gain’s dependence curve on the zenith angle and observation frequency (42). This allowed us to convert S_ν from Kelvin units to Jansky. We note that the position of this source was updated on February 15, 2024 (UT); prior to that, telescope pointing had an error of approximately 1 arcmin from the accurate location. Consequently, we corrected the flux density of these bursts using a factor derived from the beam shape of FAST’s L-band receiver (42).

The frequency-averaged specific fluence of each burst was derived by $F_\nu = S_\nu \times W_{\text{eq}}$ in units of $\text{erg cm}^{-2}\text{Hz}^{-1}$ or Jy ms. It is noted that F_ν was calculated by averaging the pulse signal over the determined frequency range of each burst, rather than the full observing bandwidth. This ap-

proach ensures that the fluence was derived solely from the emission observed within the identified frequency band. Further detailed analysis of morphological classification and drifting rate measurement will be presented in a forthcoming paper (L.-X. Zhang et al. in preparation). For further analysis on the polarization properties of this source, including the rotation measure (RM) and Faraday conversion, see the forthcoming paper (T.-C. Wang et al., in preparation). Multi-band radio observations link FRB 20240114A to a variable radio continuum source, classified as a flare radio source (FRS) rather than a persistent radio source (PRS) due to significant flux density variations (43).

We analyzed the temporal evolution of the DM, equivalent burst duration, flux density, bandwidth, and central frequency. Taking into account the uncertainties estimated using the bootstrap method, we found no significant temporal trend in any of these parameters, as shown in Fig. S1. We also carried out PCC analysis to investigate the relationship between the burst rate trend and other parameters. None of the parameter pairs displays a significant positive or negative correlation within the 95% confidence interval. These results suggest that the frequent triggering of this source has little impact on the circumburst environment or the radiation mechanism, as evidenced by the absence of significant variations in the observational parameters.

Energy Distribution

Without knowledge of the geometric beaming information of FRBs, we calculate the isotropic equivalent burst energy using the following equation similar to Refs. (44, 45):

$$E = (10^{39} \text{erg}) \frac{4\pi}{1+z} \left(\frac{D_L}{10^{28} \text{cm}} \right)^2 \left(\frac{F_\nu}{\text{Jy} \cdot \text{ms}} \right) \left(\frac{\Delta\nu}{\text{GHz}} \right), \quad (\text{S1})$$

where D_L is the luminosity distance, and $\Delta\nu$ is the bandwidth of each burst. The optimized estimates depend on the spectral shape of the burst. Since the repeating bursts typically have narrow-band emission within the observing band (20), we define F_ν as the average fluence within the frequency range specific to each burst. Accordingly, the burst energy is obtained by integrating F_ν over $\Delta\nu$, the determined bandwidth of the burst. This method allows for energy estimation without relying on any assumptions about emission outside the observing band, and thus leads to a more conservative estimate. The D_L of FRB 20240114A is estimated to be 633.87 Mpc based on the standard Planck cosmological model (46), corresponding to a spectroscopic redshift of $z = 0.1306$ (47).

The burst rate distribution as a function of energy is weighted by observation time, as the duration of individual observation sessions varies. We fit the distribution above varying energy thresholds, starting from the peak energy, using a single power-law function, as shown in Fig. 3C. The resulting power-law index displays a decreasing trend with increasing energy threshold, indicating that the PL model does not provide a good fit to the data—even above the characteristic energy.

We then fit the distribution using both LN and Bi-LN model. The residuals of the LN model, shown in Fig. 3D, reveal systematic structures in both the low- and high-energy regions, indicating that the LN model does not adequately describe the data. To quantify the model performance, we calculate the PCC between the observed and fitted values above varying energy thresholds and normalize it by the maximum PCC of each model. This approach allows us to assess the degree to which each model deviates from the observational data. We estimate the 95% probability interval of the normalized PCC for the LN model using the Monte Carlo method with 10,000 trials. The normalized PCC for the LN model shows a significant decline on both sides of the characteristic energy, exceeding its 95% probability interval.

To further evaluate the goodness of each fit, we calculate the adjusted coefficient of determination \bar{R}^2 and the reduced chi-squared statistic χ^2 and perform Akaike information criterion (AIC) (48) using the following expressions:

$$\bar{R}^2 = 1 - \frac{\sum_i^n (N_{\text{obs},i} - N_{\text{mod},i})^2}{\sum_i^n (N_{\text{obs},i} - \bar{N})^2} \left(\frac{n-1}{n-p-1} \right), \quad (\text{S2})$$

$$\chi^2 = \frac{1}{n-p} \sum_{i=1}^n \left[\frac{(N_{\text{obs},i} - N_{\text{mod},i})^2}{\sigma_i^2} \right], \quad (\text{S3})$$

$$\text{AIC} = -2 \log \mathcal{L} + 2p, \quad (\text{S4})$$

where n denotes the number of bins, p is the number of the free parameters of each model, $N_{\text{obs},i}$ is the observed value for the i th bin, $N_{\text{mod},i}$ is the fitted value for the i th bin, σ_i^2 is the error for the i th bin, estimated and transferred from the Poisson counting error of the statistical counts of each day, and $\log \mathcal{L}$ is the maximized value of the likelihood function for the model. The best-fitting parameters and statistical test results for the two models are listed in Supplementary Table S3. The adjusted R^2 , reduced χ^2 , and AIC values indicate that the LN model does not adequately describe the data, while the Bi-LN model provides a more plausible representation of the energy distribution for this source. The flat tail of the cumulative energy function, analyzed together with data from the

Kunming 40-Meter Radio Telescope (KM40M) in the S-band, is discussed in a separate paper (49).

Energy Budget Constraint

The isotropic equivalent energy of individual bursts we derived earlier is based on isotropic emission assumption. Coherent radiation from the individual FRB burst generally has a small solid angle $\delta\Omega$. Considering some bursts may exist in directions that are not observable, we introduce the emission beam to be $\Delta\Omega$, and the global beaming factor $F_b = \frac{\Delta\Omega}{4\pi}$ (27). Assuming the burst remains active at the average burst rate during the spanning time of our observation campaign, the total source energy should be written as

$$E_{\text{src}} = E_b \times F_b \times \eta_r^{-1} \times \zeta^{-1}, \quad (\text{S5})$$

where E_b denotes the total radio energy of the bursts we observed, η_r is the radio radiation efficiency, and ζ is the duty cycle of observations during the observation campaign. Supplementary Table S4 shows the total source energy estimations of this source and other five repeaters using FAST observations reported in Ref. (16–20). Assuming $\eta_r = 10^{-4}\eta_{r,-4}$ and $F_b = 0.1F_{b,-1}$, the total source energy of FRB 20240114A during the 214-day period is

$$E_{\text{src}} = (1.47 \times 10^{47} \text{ erg}) F_{b,-1} \eta_{r,-4}^{-1} (\zeta/0.0066)^{-1}, \quad (\text{S6})$$

which corresponds to $\sim 86.2\%$ of the total dipolar magnetic energy $E_{\text{mag}} = (1/6)B^2R^3 \simeq (1.7 \times 10^{47} \text{ erg}) B_{15}^2 R_6^3$ for a typical magnetar with a magnetic field $B = 10^{15}$ G and radius $R = 10^6$ cm. The magnetic moment of a magnetar is related to its magnetic field and radius by the relation $\mu = BR^3$. Here we derive the lower limit of μ as $4.7 \times 10^{32} F_{b,-1}^{1/2} \eta_{r,-4}^{-1/2} (\zeta/0.0066) R_6^{3/2}$ G cm³. A central magnetar with a magnetic moment below this threshold would be unable to supply sufficient energy to power the source with magnetic energy alone. It is the most stringent constraint on the available magnetar energy and magnetic moment, suggesting that the dipolar magnetic energy of the magnetar would be completely depleted in only ~ 250 days if the radio efficiency is indeed as low as 10^{-4} . Such a stringent energy budget constraint poses significant challenges to certain magnetar models, particularly low-efficiency models involving relativistic shocks, as well as models with large beaming factors that rely on mechanisms triggered in various regions of the magnetar.

Waiting Time

The burst arrival times were measured at the half-fluence position of each burst. We then converted the site arrival times to TCB at the infinite frequency using the software package TEMPO2 (50). We calculated the waiting time between two adjacent bursts as $\delta t = t_{i+1} - t_i$, where t_{i+1} and t_i are the barycentered arrival times for the $(i + 1)$ th and (i) th bursts, respectively. All waiting times were calculated for bursts within the same observing session to avoid long gaps of days. In Fig. S2a, the waiting time distribution exhibits a prominent bimodal characteristic with two distinct time scales, featuring peaks around 7.11 seconds and 34 milliseconds. Both components are well described by a bimodal log-normal distribution with $\bar{R}^2 = 0.983$. The bimodal log-normal distribution provides a left peak of the waiting time near 34 ms, which is quite similar to FRB 20201124A (39 ms in Ref. (18) and 51 ms in Ref. (19)) and FRB 20220912A (51 ms in Ref. (20)). The presence of closely spaced characteristic waiting times among repeating bursts may reflect intrinsic properties of the FRB source, such as the parameters of the aftershock activation function in the rotation-modulated starquake model (51). The right peak of the waiting time represents the activity of the FRB source during the statistical period.

We also analyzed whether the distribution of waiting times has a fluence dependence. The distributions of waiting time in fluence regions of $F_\nu \leq 100$ mJy ms, 100 mJy ms $< F_\nu \leq 500$ mJy ms, and $F_\nu > 500$ mJy ms were counted and analyzed separately. In Fig. S2b, the left waiting time peaks are similar across the three groups (51.38 ms for $F_\nu \leq 100$ mJy ms, 52.93 ms for 100 mJy ms $< F_\nu \leq 500$ mJy ms, and 36.78 ms for $F_\nu > 500$ mJy ms) while the offset of the right peaks (22.86 s, 11.19 s, and 18.07 s, respectively) can be attributed to the differences in burst rates across the fluence ranges. Consequently, no significant variation is observed in the left peak of the waiting time distribution across different fluence domains, though a modulation appears in the right peak. A further periodicity analysis in the time domain will be presented in an upcoming paper (D. Zhou et al., in preparation).

Comprehensive Analysis

We present a detailed, comprehensive analysis on potential correlations among various measured parameters of FRB 20240114A (see Supplementary Table S2 for the full catalog) in this section.

We investigate the potential correlation among various key parameter pairs of the bursts, which include the DM, central frequency, bandwidth, equivalent burst duration, peak flux density, and isotropic equivalent energy, aiming to gain further insights into the triggering and the emission mechanism of repeating FRBs.

Fig. S3 shows the pair-wise correlation analysis between the measured parameters of FRB 20240114A. Notably, the bandwidth-central frequency plane displays a triangular shape, as the central frequency marks the midpoint of the observed frequency range. There is no obvious correlation among most parameter pairs, except for the peak flux density-isotropic equivalent energy, the bandwidth-isotropic equivalent energy, and the equivalent burst duration-isotropic equivalent energy planes, which arise from parameter coupling. Therefore, most of the parameters are incoherent with each other.

We calculate the PCC for each of the parameter pairs, which reveals that only the flux density-energy plane and the bandwidth-energy plane yields PCC values higher than 0.5, with values of 0.86 and 0.67, respectively. The positive correlations can be attributed to the fact that the isotropic equivalent energy is proportional to the peak flux density and bandwidth. The W_{eq} distribution spans a relatively narrow range (within approximately one order of magnitude), whereas the peak flux density distribution extends across nearly five orders of magnitude. As a result, the energy distribution is primarily dominated by the peak flux density, leading to a stronger positive correlation in the flux-energy plane.

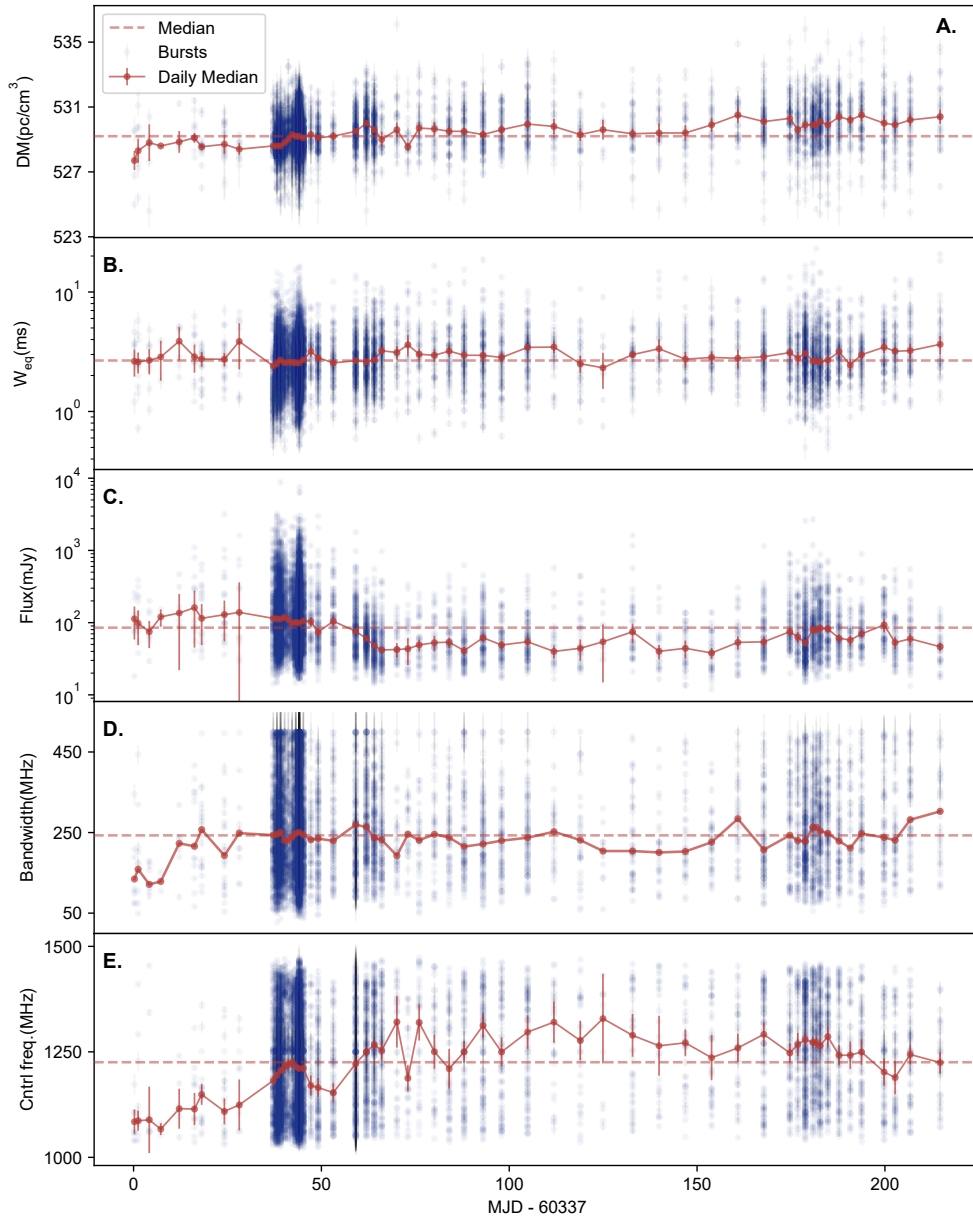


Figure S1: The temporal evolution of FRB2 0240114A. Panel A-E shows the DM, W_{eq} , flux density, bandwidth and central frequency temporal evolution of FRB 20240114A, respectively. The blue dots denote the corresponding parameter of all the bursts, the red represent the median value of the corresponding parameter in each observation session. The error bars represent the uncertainty in the median of each parameter. The red dashed lines shows the median value of all bursts for each parameter.

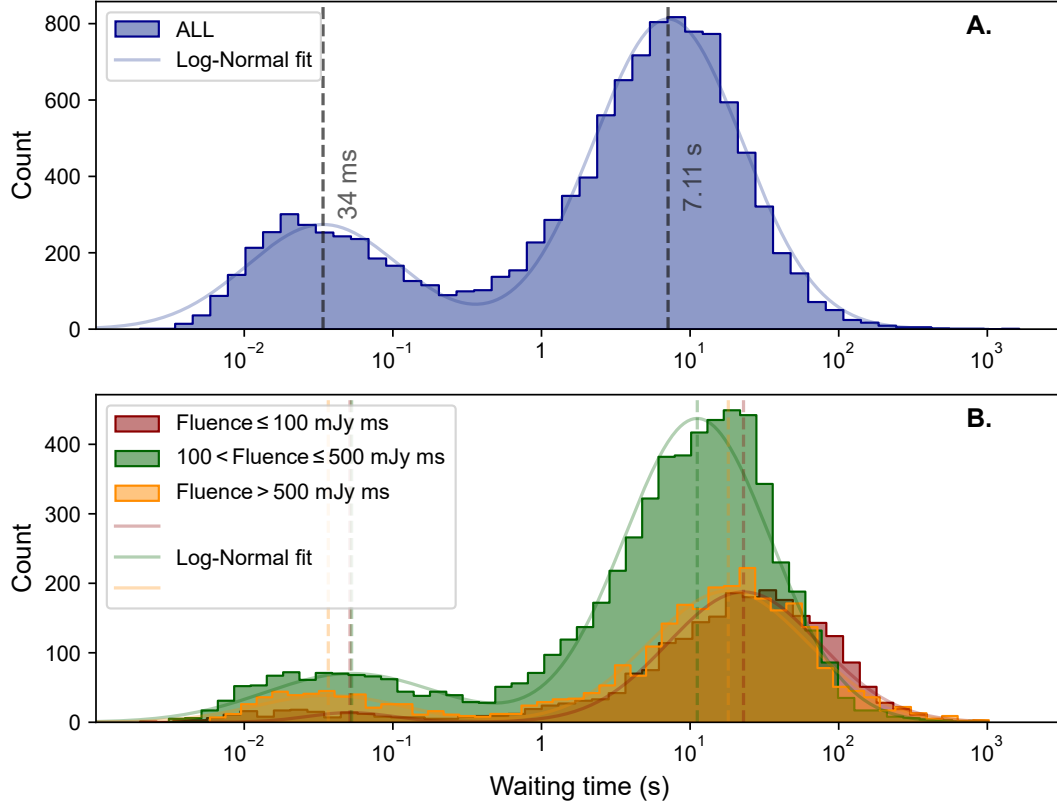


Figure S2: The waiting time distribution of FRB 20240114A. Panel A: The blue bars denote the waiting time histograms of all the bursts from FRB 20240114A. The blue solid line is the best-fit model with two log-normal functions. The dashed lines indicate the locations of maximum values in the two log-normal functions. The longer timescale peak is centered around 7.11 s, while the shorter timescale peak is at 34 ms. Panel B: The waiting time distributions are shown for three distinct energy ranges. The red, green, and orange bars correspond to bursts with energies of $F_\nu \leq 100$ mJy ms, $100 \text{ mJy ms} < F_\nu \leq 500$ mJy ms, and $F_\nu > 500$ mJy ms, respectively. For each case, the corresponding solid lines denote the best-fit models, and the corresponding dashed lines indicate the peak locations for the respective distributions.

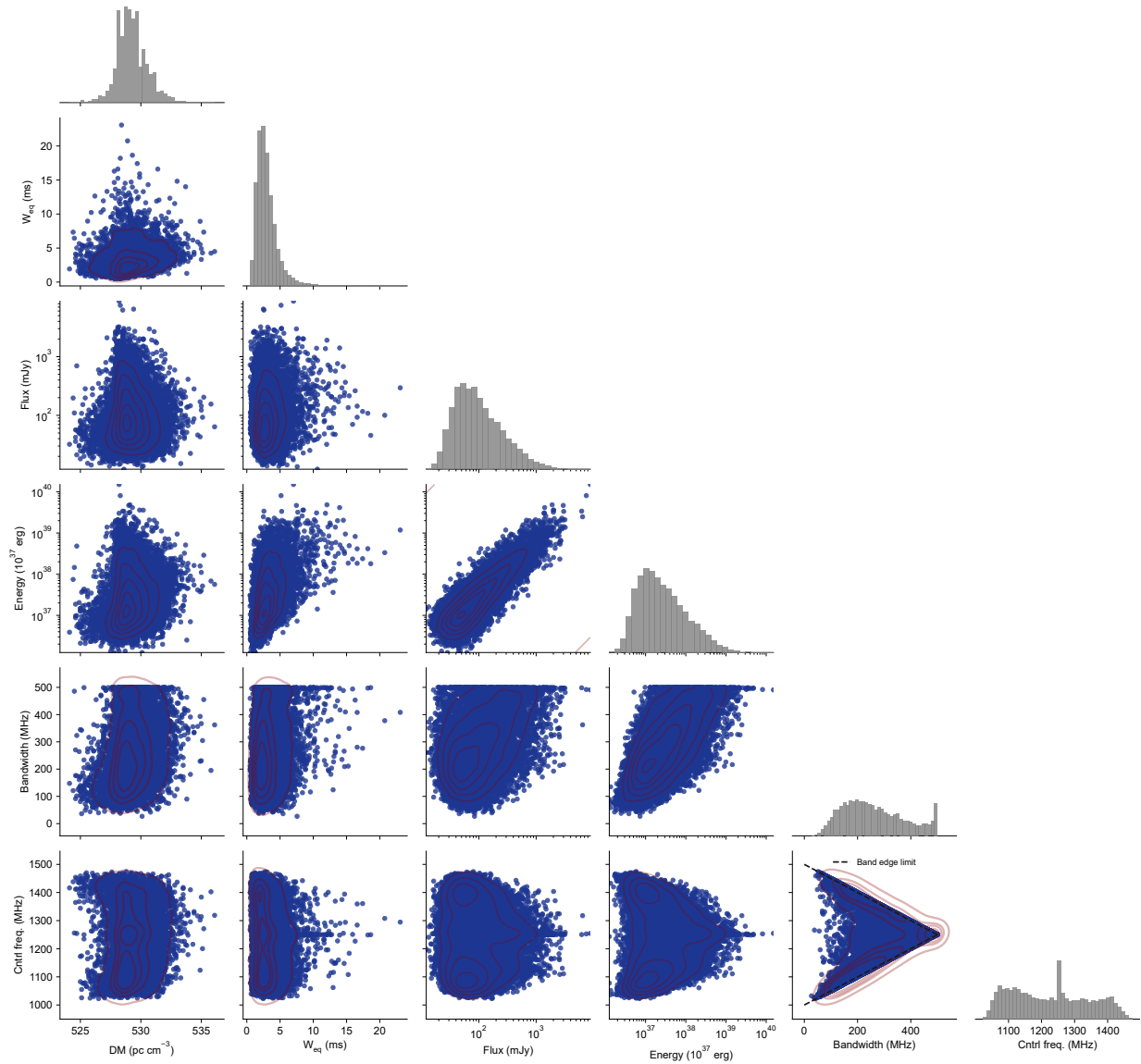


Figure S3: The pairwise correlation analysis between the observation properties of the bursts. The blue dots represent the parameters of each burst. The red contour lines present in each panel are the result of the KDE fitting. The gray histograms represent the parameter distributions of the bursts. The dashed black triangular shape in the Bandwidth-Central frequency panel is due to the limits of our observing band.

Table S1: Observations of FRB 20240114A from Jan. 2024 to Aug. 2024.

| Date UT (YYYYMMDD) | MJD _{start} ^a (at infinite freq.) | MJD _{end} ^b (at infinite freq.) | Freq. resolution (kHz) | t _{samp} (μ s) | Duration (hour) | Num. of Detections | Burst Rate ^c (hour ⁻¹) |
|-----------------------|--|--|---------------------------|---------------------------------|--------------------|-----------------------|--|
| 20240128 | 60337.229849817 | 60337.250683150 | 122.070 | 196.608 | 0.50 | 8 | 16.0 |
| 20240129 | 60338.215266484 | 60338.236099817 | 122.070 | 49.152 | 0.50 | 11 | 22.0 |
| 20240201 | 60341.179849817 | 60341.200683150 | 122.070 | 49.152 | 0.50 | 9 | 18.0 |
| 20240204 | 60344.240960928 | 60344.261794262 | 122.070 | 49.152 | 0.50 | 2 | 4.0 |
| 20240209 | 60349.152766484 | 60349.173599817 | 122.070 | 49.152 | 0.50 | 6 | 12.0 |
| 20240213 | 60353.215960928 | 60353.236794262 | 122.070 | 49.152 | 0.50 | 14 | 28.0 |
| 20240215 | 60355.131238706 | 60355.152072039 | 122.070 | 49.152 | 0.50 | 21 | 42.0 |
| 20240221 | 60361.179155373 | 60361.199988706 | 122.070 | 49.152 | 0.50 | 24 | 48.0 |
| 20240225 | 60365.131933150 | 60365.152766484 | 122.070 | 49.152 | 0.50 | 11 | 22.0 |
| 20240305 | 60374.188183150 | 60374.209016484 | 61.035 | 98.304 | 0.50 | 225 | 450.0 |
| 20240306 | 60375.134710928 | 60375.218044262 | 122.070 | 49.152 | 2.00 | 918 | 459.0 |
| 20240307 | 60376.102766484 | 60376.186099817 | 122.070 | 49.152 | 2.00 | 969 | 484.5 |
| 20240308 | 60377.193044262 | 60377.221447039 | 122.070 | 49.152 | 0.68 | 347 | 509.0 |
| 20240309 | 60378.191655373 | 60378.205660002 | 122.070 | 49.152 | 0.34 | 186 | 553.4 |
| 20240310 | 60379.199294262 | 60379.219120650 | 122.070 | 49.152 | 0.48 | 270 | 567.4 |
| 20240311 | 60380.152766484 | 60380.194433150 | 122.070 | 49.152 | 1.00 | 727 | 727.0 |
| 20240312 | 60381.038183150 | 60381.220822039 | 122.070 | 49.152 | 4.38 | 3197 | 729.4 |
| 20240313 | 60382.173599817 | 60382.215266484 | 122.070 | 49.152 | 1.00 | 535 | 535.0 |
| 20240315 | 60384.190960928 | 60384.204849817 | 122.070 | 49.152 | 0.33 | 66 | 198.0 |
| 20240317 | 60386.118738706 | 60386.139572039 | 122.070 | 49.152 | 0.50 | 171 | 342.0 |
| 20240321 | 60390.158322039 | 60390.172210928 | 61.035 | 98.304 | 0.33 | 111 | 333.0 |
| 20240327 | 60396.133322039 | 60396.154155373 | 122.070 | 49.152 | 0.50 | 297 | 594.0 |
| 20240329 | 60398.981933150 | 60399.002766484 | 122.070 | 49.152 | 0.50 | 275 | 550.0 |
| 20240401 | 60401.066655373 | 60401.087488706 | 122.070 | 49.152 | 0.50 | 261 | 522.0 |
| 20240403 | 60403.046516484 | 60403.067349817 | 122.070 | 49.152 | 0.50 | 141 | 282.0 |
| 20240407 | 60407.091655373 | 60407.112488706 | 122.070 | 49.152 | 0.50 | 41 | 82.0 |
| 20240410 | 60410.020822039 | 60410.041655373 | 122.070 | 49.152 | 0.50 | 35 | 70.0 |
| 20240413 | 60413.023599817 | 60413.044433150 | 122.070 | 49.152 | 0.50 | 44 | 88.0 |
| 20240417 | 60417.078460928 | 60417.099294262 | 122.070 | 49.152 | 0.50 | 45 | 90.0 |
| 20240421 | 60421.009016484 | 60421.029849817 | 122.070 | 49.152 | 0.50 | 72 | 144.0 |
| 20240424 | 60424.983322039 | 60425.004155373 | 122.070 | 49.152 | 0.50 | 110 | 220.0 |
| 20240430 | 60430.029155373 | 60430.049988706 | 122.070 | 49.152 | 0.50 | 133 | 266.0 |
| 20240504 | 60434.956933150 | 60434.977766484 | 122.070 | 49.152 | 0.50 | 89 | 178.0 |
| 20240511 | 60441.888877595 | 60441.909710928 | 122.070 | 49.152 | 0.50 | 102 | 204.0 |

| Date UT (YYYYMMDD) | MJD ^a _{start} (at infinite freq.) | MJD ^b _{end} (at infinite freq.) | Freq. resolution (kHz) | t _{samp} (μ s) | Duration (hour) | Num. of Detections | Burst Rate ^c (hour ⁻¹) |
|-----------------------|--|--|---------------------------|---------------------------------|--------------------|-----------------------|--|
| 20240518 | 60448.897210928 | 60448.911099817 | 122.070 | 49.152 | 0.33 | 32 | 96.0 |
| 20240525 | 60455.913877595 | 60455.927766484 | 122.070 | 49.152 | 0.33 | 37 | 111.0 |
| 20240531 | 60461.949294262 | 60461.963183150 | 122.070 | 49.152 | 0.33 | 11 | 33.0 |
| 20240608 | 60469.827766484 | 60469.841655373 | 122.070 | 49.152 | 0.33 | 49 | 147.0 |
| 20240615 | 60476.877072039 | 60476.890960928 | 122.070 | 49.152 | 0.33 | 29 | 87.0 |
| 20240622 | 60483.881933150 | 60483.895822039 | 122.070 | 49.152 | 0.33 | 40 | 120.0 |
| 20240629 | 60490.862488706 | 60490.876377595 | 122.070 | 49.152 | 0.33 | 46 | 138.0 |
| 20240706 | 60497.858322039 | 60497.872210928 | 122.070 | 49.152 | 0.33 | 42 | 126.0 |
| 20240713 | 60504.761099817 | 60504.774988706 | 122.070 | 49.152 | 0.33 | 117 | 351.0 |
| 20240720 | 60511.684710928 | 60511.698599817 | 122.070 | 49.152 | 0.33 | 100 | 300.0 |
| 20240722 | 60513.800683150 | 60513.815266484 | 122.070 | 49.152 | 0.35 | 92 | 262.9 |
| 20240724 | 60515.773599817 | 60515.834710928 | 61.035 | 98.304 | 1.47 | 369 | 251.6 |
| 20240726 | 60517.819433150 | 60517.840266484 | 122.070 | 49.152 | 0.50 | 166 | 332.0 |
| 20240727 | 60518.742349817 | 60518.756238706 | 122.070 | 49.152 | 0.33 | 92 | 276.0 |
| 20240728 | 60519.765266484 | 60519.786099817 | 122.070 | 49.152 | 0.50 | 208 | 416.0 |
| 20240730 | 60521.799988706 | 60521.820822039 | 122.070 | 49.152 | 0.50 | 138 | 276.0 |
| 20240802 | 60524.783322039 | 60524.797210928 | 122.070 | 49.152 | 0.33 | 108 | 324.0 |
| 20240805 | 60527.777766484 | 60527.791655373 | 122.070 | 49.152 | 0.33 | 52 | 156.0 |
| 20240808 | 60530.774988706 | 60530.788877595 | 122.070 | 49.152 | 0.33 | 90 | 270.0 |
| 20240814 | 60536.777766484 | 60536.791655373 | 122.070 | 49.152 | 0.33 | 86 | 258.0 |
| 20240817 | 60539.709710928 | 60539.723599817 | 122.070 | 49.152 | 0.33 | 70 | 210.0 |
| 20240821 | 60543.737488706 | 60543.751377595 | 122.070 | 49.152 | 0.33 | 66 | 198.0 |
| 20240829 | 60551.699294262 | 60551.713183150 | 122.070 | 49.152 | 0.33 | 40 | 120.0 |

^a The start time of each observation session with topocentric coordinates, corrected to infinite frequency.

^b The end time of each observation session with topocentric coordinates, corrected to infinite frequency.

^c The burst rate is assumed to be a constant throughout the day, defined as the number of detections divided by the duration of observation.

Table S2: The properties of 11,553 bursts of FRB 20240114A measured with FAST^a.

| Burst ID | MJD ^b _{bary} (at infinite freq.) | DM ^c (pc cm ⁻³) | W _{eq} ^d (ms) | Cntrl freq. ^e (MHz) | Bandwidth ^f (MHz) | Peak flux ^g (mJy) | Fluence (mJy ms) | Energy ^h _{Δν} (×10 ³⁷ erg) |
|----------|---|---|--------------------------------------|-----------------------------------|---------------------------------|---------------------------------|---------------------|--|
| B00001 | 60337.233896015 | 529.5±0.1 | 3.51±0.23 | 1105 | 188±11 ³⁾ | 217.5±9.6 | 764±61 | 6.12±0.60 |
| B00002 | 60337.235854917 | 529.6±0.8 | 2.60±0.43 | 1041 | 75±8 ²⁾ | 86.5±3.8 | 225±39 | 0.72±0.15 |
| B00003 | 60337.237146105 | 525.0±0.3 | 4.63±1.23 | 1167 | 355±67 ³⁾ | 18.1±0.9 | 84±23 | 1.27±0.42 |
| B00004 | 60337.239375175 | 526.7±2.0 | 2.66±0.49 | 1039 | 74±5 ²⁾ | 74.3±3.3 | 198±38 | 0.62±0.13 |
| B00005 | 60337.239452224 | 527.0±2.2 | 1.20±0.26 | 1064 | 104±4 ³⁾ | 77.4±3.6 | 93±21 | 0.41±0.09 |
| B00006 | 60337.243643750 | 527.7±0.2 | 3.67±0.38 | 1058 | 111±11 ²⁾ | 127.5±4.9 | 468±52 | 2.20±0.33 |
| B00007 | 60337.245743427 | 527.7±0.1 | 3.02±0.21 | 1106 | 208±6 ²⁾ | 257.9±11.6 | 780±65 | 6.88±0.61 |
| B00008 | 60337.246124366 | 526.8±0.3 | 3.72±0.53 | 1058 | 99±14 ³⁾ | 98.2±4.5 | 365±55 | 1.53±0.32 |
| B00009 | 60338.212964888 | 528.5±0.1 | 1.62±0.06 | 1291 | 319±8 ²⁾ | 224.6±7.9 | 363±19 | 4.93±0.29 |
| B00010 | 60338.216853487 | 527.9±0.1 | 5.75±1.02 | 1100 | 228±37 ³⁾ | 37.8±0.8 | 217±39 | 2.10±0.51 |
| ... | ... | ... | ... | ... | ... | ... | ... | ... |
| B11543 | 60551.715922689 | 528.6±0.2 | 5.51±0.80 | 1392 | 389±23 ³⁾ | 30.8±2.9 | 170±29 | 2.80±0.52 |
| B11544 | 60551.716676723 | 530.4±0.1 | 2.02±0.11 | 1220 | 407±11 ²⁾ | 82.9±7.6 | 167±18 | 2.90±0.32 |
| B11545 | 60551.716689314 | 528.4±0.3 | 2.41±0.23 | 1395 | 171±16 ²⁾ | 69.1±6.0 | 167±21 | 1.21±0.19 |
| B11546 | 60551.716691701 | 532.1±0.1 | 9.38±0.37 | 1144 | 249±50 ¹⁾ | 115.2±10.3 | 1081±106 | 11.45±2.55 |
| B11547 | 60551.716691923 | 533.0±0.3 | 8.35±0.32 | 1133 | 243±5 ²⁾ | 132.2±11.5 | 1104±105 | 11.39±1.11 |
| B11548 | 60551.717399910 | 529.2±1.6 | 6.99±1.65 | 1206 | 198±6 ³⁾ | 17.5±1.5 | 122±31 | 1.03±0.26 |
| B11549 | 60551.718067969 | 533.2±0.7 | 3.22±0.35 | 1274 | 172±5 ³⁾ | 42.1±3.5 | 135±19 | 0.99±0.14 |
| B11550 | 60551.718584716 | 529.3±0.5 | 2.55±0.52 | 1251 | 480±25 ³⁾ | 17.9±1.6 | 46±10 | 0.94±0.21 |
| B11551 | 60551.718678457 | 528.3±1.5 | 2.53±0.54 | 1071 | 116±7 ²⁾ | 29.9±2.6 | 76±17 | 0.37±0.09 |
| B11552 | 60551.718785581 | 533.2±0.2 | 5.73±0.39 | 1194 | 340±11 ²⁾ | 64.0±6.0 | 366±42 | 5.30±0.63 |
| B11553 | 60551.718925823 | 530.2±1.4 | 4.34±0.84 | 1218 | 394±79 ¹⁾ | 20.1±1.8 | 87±18 | 1.46±0.42 |

^a The full table is available in ScienceDB, doi: <https://doi.org/10.57760/sciencedb.Fastro.00030>.^b Arrival time of burst peak at the solar system barycenter, after correcting to the infinite frequency.^c DM obtained from the best burst alignment. A '-' is marked and the daily averaged DM value is used where the DM-fit failed.^d The equivalent width W_{eq} was defined as the width of a rectangular burst that has the same area as the profiles, with the height of peak flux density.^e The central frequency is defined as the median value of the frequency range of the burst.^f Three types of burst bandwidth fit were considered: #1) Boxcar bandwidth of the burst with complex morphological structures or those that were too faint. A conservative 20% fractional error is assumed; #2) CDF frequency boundaries of the bursts, the uncertainty of measurement was estimated using the bootstrap method; #3) A frequency extended Gaussian fit was used to correct the bandwidth for the bursts' cut off by the upper/lower limit of the observed frequency, 1σ measuring uncertainty.^g The average peak flux density over their individual frequency range of bursts. A '*' indicates bursts affected by saturation, which may lead to a potential underestimation of their flux density.^h The isotropic energy of the bursts was calculated using a measured frequency bandwidth, see text.

Table S3: The fitted parameters of the burst rate distribution of energy

| Model | Fitting parameter | \bar{R}^2 | Reduced χ^2 | AIC |
|-------|--|-------------|------------------|-------|
| LN | $E_c = 1.71 \times 10^{37}$ erg, $\sigma = 0.57$ | 0.918 | 13.38 | 58.00 |
| Bi-LN | $E_{c1} = 1.00 \times 10^{37}$ erg, $\sigma_1 = 0.56$ $E_{c2} = 3.87 \times 10^{37}$ erg, $\sigma_2 = 0.31$ | 0.986 | 2.38 | 13.64 |

Table S4: The energy budgets of five repeating FRBs.

| FRB Name | Duty Cycle ^a | Radio E ^b | Averaged E ^c | Source E ^d |
|------------------------|-------------------------|-----------------------|-------------------------|------------------------------------|
| | ζ | (erg) | (erg hr ⁻¹) | ($\eta_{r,-4}^{-1} F_{b,-1}$ erg) |
| 20121102A | 0.053 | 1.36×10^{41} | 2.29×10^{39} | 2.59×10^{45} |
| 20190520B | 0.070 | 4.39×10^{39} | 2.37×10^{38} | 6.26×10^{43} |
| 20201124A ^e | 0.063 | 1.65×10^{41} | 2.01×10^{39} | 2.60×10^{45} |
| 20201124A ^f | 0.042 | 6.42×10^{40} | 1.60×10^{40} | 1.54×10^{45} |
| 20220912A | 0.021 | 7.42×10^{40} | 8.55×10^{39} | 3.49×10^{45} |
| 20240114A | 0.0066 | 9.62×10^{41} | 2.84×10^{40} | 1.47×10^{47} |

^a The observation duty cycle, e.g., for FRB 20240114A in this paper, the duty cycle is 33.86 hours out of 214 days.

^b Sum of the observed isotropic radio energies of all bursts.

^c The total radio energy divided by observation time, e.g. for FRB 20240114A in this paper, the averaged energy is 9.62×10^{41} erg / 33.86 hours.

^d The total source energy calculated with Eq. S5, using $\eta_r = 10^{-4} \eta_{r,-4}^{-1}$ and $F_b = 0.1 F_{b,-1}$.

^e FAST observation of FRB 20201124A in 2021.04 by Ref. (18)

^f FAST observation of FRB 20201124A in 2021.09 by Ref. (19)